Biophysical Journal
Article

Biophysical Society

Cellular Stiffness as a Novel Stemness Marker in the Corneal Limbus

Tom Bongiorno,[1] Jena L. Chojnowski,[2] James D. Lauderdale,[2] and Todd Sulchek[1,3,*]
[1]The G. W. Woodruff School of Mechanical Engineering, Georgia Institute of Technology, Atlanta, Georgia; [2]Department of Cellular Biology, University of Georgia, Athens, Georgia; and [3]The Parker H. Petit Institute for Bioengineering and Bioscience, Georgia Institute of Technology, Atlanta, Georgia

ABSTRACT Healthy eyes contain a population of limbal stem cells (LSCs) that continuously renew the corneal epithelium. However, each year, 1 million Americans are afflicted with severely reduced visual acuity caused by corneal damage or disease, including LSC deficiency (LSCD). Recent advances in corneal transplant technology promise to repair the cornea by implanting healthy LSCs to encourage regeneration; however, success is limited to transplanted tissues that contain a sufficiently high percentage of LSCs. Attempts to screen limbal tissues for suitable implants using molecular stemness markers are confounded by the poorly understood signature of the LSC phenotype. For cells derived from the corneal limbus, we show that the performance of cell stiffness as a stemness indicator is on par with the performance of ΔNP63α, a common molecular marker. In combination with recent methods for sorting cells on a biophysical basis, the biomechanical stemness markers presented here may enable the rapid purification of LSCs from a heterogeneous population of corneal cells, thus potentially enabling clinicians and researchers to generate corneal transplants with sufficiently high fractions of LSCs, regardless of the LSC percentage in the donor tissue.

INTRODUCTION

Each year, more than 1 million Americans suffer impaired eyesight resulting from cornea damage, which may arise from either a congenital cause, such as aniridia-related keratopathy, or an acquired cause, such as chemical or blast injury or Stevens-Johnson syndrome (1). The resulting dysfunction of limbal stem cells (LSCs), a population of stem cells that are located in the basal epithelium at the corneoscleral limbus and maintain the cornea, has been recognized as a major cause of prolonged visual loss and blindness (2,3). Such LSC dysfunction results in LSC deficiency (LSCD), a disease characterized by the loss of corneal integrity and impaired corneal wound healing that can result in blindness (reviewed in (4)).

Current treatments for LSCD typically entail transplantation of tissue from allogeneic or autologous donors (5). Transplants sourced from allogeneic donors are limited by the high risk of immunorejection and the general necessity of a life-long immunosuppressive drug regimen (3). Autologous transplantations are beneficial for unilateral conditions, which typically result from traumatic eye injury, but have limited benefit in the treatment of bilateral congenital eye diseases (6). Interestingly, the clinical success of transplantation depends on not only the total number but also the percentage of stem cells in the graft (7). Transplant success was found to substantially improve when LSCs, defined as ΔNP63α-positive, holoclone-forming cells, comprised $\geq$3% of the transplanted cells (8), further illustrating the importance of sufficiently high LSC percentages. However, the ex vivo expansion and transplantation of autologous limbal tissue acquired from a contralateral biopsy is fettered by the laborious collection of sufficiently high numbers and percentages of transplanted LSCs (8–10), which must be performed rapidly to ensure cell viability. Furthermore, the high patient-to-patient variability in the starting percentage of LSCs taken from a tissue biopsy diminishes the utility of ex vivo culturing to treat LSCD with stem cells (8). Cell-enrichment techniques are therefore vital for improving the treatment of LSCD.

Current enrichment methods, which are based on the use of antibodies to select for limbal stem or progenitor cells, include magnetic bead capture and flow cytometry (11–13). Such immunologically based cell-enrichment techniques, while useful, are limited by the need for appropriate

Submitted March 22, 2016, and accepted for publication September 2, 2016.
*Correspondence: todd.sulchek@me.gatech.edu
Tom Bongiorno and Jena L. Chojnowski contributed equally to this work.
Editor: Jochen Guck.
http://dx.doi.org/10.1016/j.bpj.2016.09.005

cell-type-specific antibodies. Antibodies against the ATP-binding cassettes subfamily G member 2 (ABCG2) and subfamily B member 5 (ABCB5) have been successfully used to enrich the LSC population, but they also enrich for other ABCG2- or ABCB5-expressing cells present in the limbus and cornea (11,14–16). The use of antibodies to identify LSCs in the clinic is cumbersome, requiring ~15 h of laborious cell processing, and can subsequently affect cellular physiology if the epitope is associated with a functionally important protein domain (17–19). A label-free microfluidic device that sorts based on cellular biomechanical properties offers cost and labor advantages over current methods and may provide sufficient enrichment to serve as an alternative or additional approach to antibody-based techniques. Therefore, coupled with label-free cell-enrichment approaches, the identification of new biophysical markers of LSCs could greatly improve LSCD treatment by enabling a faster and cheaper process to collect stem-like cells.

Recently, various cell mechanical properties, including stiffness (i.e., Young's modulus) and size, have been shown to distinguish stem cell phenotypes from differentiated cells at the single-cell level for various stem cell types (20–24). Changes in biomechanical properties during stem cell differentiation could enable microfluidic approaches for on-the-fly analysis and sorting of stem cells from differentiated cells. Although LSCs have been characterized by a small diameter and high nucleus/cytoplasm ratio in comparison with other cells from the limbal region (14,21,25), a complete biophysical characterization of LSCs in relation to the surrounding corneal cells has not yet been achieved.

We present a complete analysis of LSC mechanics in congruence with the progenitor marker ΔNP63α, which is expressed in LSCs and progenitor cells, but not differentiated cells. The results indicate that cell deformability represents a distinct biophysical marker for stemness identification of cells derived from the corneal limbus. Thus, cell mechanical properties can potentially be used as phenotypic markers for rapid, label-free, microfluidic enrichment of LSCs from corneal tissue as a step toward improving the clinical treatment of LSCD patients.

MATERIALS AND METHODS

Cell isolation and cell culture

Human limbal epithelial cells (LECs) were obtained from Life Technologies (Carlsbad, CA; #C-018-5C). Each lot was characterized by the manufacturer as positive for cytokeratin 15 and ΔNP63α immunofluorescent staining. The cells were thawed and cultured as described by the manufacturer. LECs were maintained in culture media with a low calcium concentration (30 μM) as previously described (26).

At passage 0, the undifferentiated LECs were stained for ΔNP63α and ABCG2 (LEC lot 1645759) or mechanically characterized by atomic force microscopy (AFM; LEC lot 1163447). Differentiated LECs were obtained by long-term in vitro culture (4 weeks, 2 passages; LEC lot 1163447). The differentiated LECs were either stained for ΔNP63α and ABCG2 or mechanically characterized.

The central cornea was dissected from a 70-year-old cadaveric human cornea within 36 h postmortem (Georgia Eye Bank, IRB #10336-4). To obtain a dissociated cell suspension, the corneal tissue was cut into 2- to 4-mm pieces and incubated with 2.4 units/mL of Dispase II (Roche Diagnostics, Risch-Rotkreuz, Switzerland) for 1 h at 37°C. Cells were recovered by incubation with 0.5 M EDTA (Invitrogen, Carlsbad, CA) for 10 min at 37°C, and enzymatic activity was arrested by the addition of serum-containing media.

Immunohistochemistry

LECs and differentiated LECs were adhered to glass coverslips, fixed with 4% paraformaldehyde, permeabilized in a buffer containing 0.5% Triton X-100, and blocked with 6% donkey serum and 0.3% Triton X-100 at room temperature for 1 h. Slides were incubated with primary antibody against human ΔNP63α (#ab111449; 1:50; Abcam, Cambridge, United Kingdom) or ABCG2 (#ab24114; 1:20; Abcam) overnight at 4°C, washed in phosphate-buffered saline containing 0.05% Tween (PBST), and incubated with 488 or 594 DyLight-conjugated secondary antibody (1:1000; Jackson Immunoresearch, West Grove, PA) for 1 h and 4′,6-diamidino-2-phenylindole (1:10,000; DAPI) for 5 min. Images were acquired using an LSM510 confocal microscope and AxioVision image acquisition software (both from Zeiss, Jena, Germany).

Cadaveric human cornea tissue was fixed with 4% paraformaldehyde overnight. The tissue was dehydrated using an ethanol gradient (2 h each of 70%, 80%, 90%, 95%, and 100% ethanol) and then embedded in paraffin. Then, 7-μm-thick sections were prepared on a microtome, dewaxed in xylene, and rehydrated through an ethanol gradient to distilled water. The tissue sections were mounted on glass slides, covered with 0.05% trypsin solution, incubated for 5 min at 37°C, and rinsed with PBST. The sections were then stained for ΔNP63α and imaged as described above. For clarity, the central cornea images were cropped to remove the stroma.

ΔNP63α and ABCG2 image quantification

To verify the phenotype of each population, the percentage of ΔNP63α^{bright} cells was quantified (Fig. S1 *A* in the Supporting Material; LEC, $n = 335$; differentiated LEC, $n = 297$). ImageJ (National Institutes of Health, Bethesda, MD) was used to transform the images into the hue-saturation-brightness color space and extract the brightness channel of both DAPI and ΔNP63α images for further analysis. CellProfiler (27) was used to identify cell nuclei using the Otsu threshold method for the DAPI images. The ΔNP63α staining associated with each nucleus was determined using the background threshold method and the propagation method of secondary object identification (28), seeded by the previously identified nuclei. Cells with nuclei or associated ΔNP63α staining that touched the border of the image were excluded from quantification. Since images were captured under 10× or 20× magnification, the intensity of the images was normalized by NA^4/M^2, where NA and M are the numerical aperture and magnification, respectively, of the objective. Cells were defined as ΔNP63α^{bright} if the mean intensity exceeded 6.1% of the dynamic range, at which point the lower confidence interval (CI) bound of the diagnostic odds ratio (DOR) was maximal (see Figs. 2 *D* and 7 *E*). The chosen threshold thus represents the point at which the confidence in a high DOR is maximal.

Similarly, ABCG2 images were used to identify the cytoplasmic region of each cell (Fig. S1 *B*; LEC, $n = 248$; differentiated LEC, $n = 113$). The cytoplasmic area was used to quantify the diameter and aspect ratio of each cell. In combination with the nuclear area identified from the DAPI images, the cytoplasmic area was used to calculate the nucleus/cytoplasm ratio. The intact tissue images of the central cornea could not be quantified in comparison with the LECs and differentiated LECs due to

the close cell proximity, confounded by the high variability in sample thickness.

AFM

Cells were plated on poly-L-lysine-coated glass dishes and immobilized during a 16–24 h incubation at 37°C. To discourage differentiation, the LECs were immobilized in stem cell maintenance media until immediately before mechanical probing was conducted. To simplify the tip-cell contact geometry, 5.5-μm polystyrene beads were attached to tipless silica nitride cantilevers (Bruker Probes, Camarillo, CA) using two-part epoxy and dried overnight. The mechanical properties of individual cells were obtained from force-indentation curves recorded with an atomic force microscope (Asylum Research, Santa Barbara, CA) with an integrated optical microscope (Nikon, Melville, NY) on a vibration isolation table. The Sader calibration method (29) was used to obtain cantilever spring constants ($k \approx 15$ pN/nm) based on the thermal vibration of the cantilever. The positions of the z-piezo and the cantilever deflection, Δx, were acquired simultaneously (Fig. 1 *A*, *blue*) to obtain the cell indentation, δ (*red*). The force, F, exerted on the cell was calculated using the cantilever spring constant, k, by $F = k \cdot \Delta x$. A mechanical analysis of the stiffness and viscoelastic properties is illustrated for an idealized cell in Fig. 1, *B–E*.

The cantilever probe was visually aligned with the cell center and translated to indent the cell with a velocity of 2 μm/s (Fig. 1 *B*). Contact between the cantilever and the cell was indicated by an increase in indentation. The translation velocity was maintained to exert a steadily increasing compressive force on the cell until a force trigger of 5 nN was reached, completing the compression segment of the curve. To examine the cell relaxation under compression, the cantilever was allowed to dwell at the surface of the compressed cell for 1 s by setting the translation velocity to zero while recording the cellular relaxation response (relaxation segment).

Calculation of Young's modulus

The Hertzian contact model, which describes the force-indentation relationship for deformable, sphere-sphere contact (30), was employed to calculate the cellular Young's modulus (Fig. 1, *C* and *D*). The model was fit to the compression segment of the force-indentation curve over an applied force range of 2.5–4.75 nN, where the Young's modulus was largely independent of the indentation (Fig. 1 *C*, *blue dashed line*). The cells were assumed to be incompressible, such that the cellular Poisson's ratio was taken as 0.5. The Young's modulus was calculated as the average of three independent measurements taken at the same location in each cell, with a pause between measurements so that each measurement produced consistent results.

Calculation of viscoelastic relaxation constants

To calculate the viscoelastic properties of the cells, the spring-damper model was fit to the relaxation segment of the force-time curve (Fig. 1 *B*, *red dashed line*), using the Maxwell-Wiechert model to calculate the viscoelastic time constants (31) (Fig. 1 *E*). Two Maxwell elements were chosen to best fit the data. The fast and slow viscoelastic time constants were designated as τ_1 and τ_2, respectively. The viscoelastic properties of each cell were calculated as the averages of three independent measurements.

Calculation of morphological parameters

To calculate the diameter and aspect ratio of each cell based on the phase-contrast images captured immediately after AFM probing (see Fig. 3 *A*), ImageJ was employed to manually draw a polygon around each cell. The diameter was calculated as the mean of the major and minor axes of the fit ellipse, and the aspect ratio was calculated as the major axis divided by the minor axis.

Statistics and figure generation

Due to the nonnormal distribution of each biophysical parameter (Shapiro-Wilk W test, $\alpha = 0.05$), a bootstrapping ANOVA was performed using a custom MATLAB (The MathWorks, Natick, MA) code to discern statistically significant differences (heteroscedastic comparisons, 10,000 bootstrapping iterations, $\alpha = 0.05$), as previously described (20). Post hoc analyses were performed using bootstrapping Student's *t*-tests. To assess the significance of the post hoc results, Holm's adjusted *p*-values were compared with $\alpha = 0.1$.

Spearman's rank correlation coefficients were used to assess the relationship between pairs of mechanical properties measured at the single-cell level (LEC, $n = 36$; central cornea, $n = 40$; differentiated LEC, $n = 60$). Coefficients and raw *p*-values were obtained using JMP statistical software (SAS Institute, Cary, NC), and a custom Microsoft Excel spreadsheet was used to apply the Holm's adjustment and plot the resulting color matrices (see Fig. 5 *B*). Beeswarm plots (e.g., Fig. 2 *D*) and semitransparent scatter plots (Fig. 5 *A*) were generated using custom MATLAB codes.

Classifier analysis

To assess the utility of the mechanical parameters as stemness indicators in comparison with conventional markers, each parameter was tested for its ability to distinguish stem-like from differentiated phenotypes. As prevalence-independent measurements, the true-positive rate (TPR), false-positive rate (FPR), and DOR were chosen to assess the binary classification of cells based on the parameters measured in this study. To visualize the impact of the threshold value on the utility of each classifier, receiver operating characteristic (ROC) curves were plotted by comparing the TPR and FPR for the full range of threshold values (see Fig. 6, *A–C*). The 95% CIs of the ROC curves were calculated by bootstrapping using a custom MATLAB code. The CI bounds of the DOR were calculated by $\mathrm{DOR} \pm \mathrm{CI} = e^{\ln(\mathrm{DOR}) \pm a\sqrt{(1/\mathrm{TP})+(1/\mathrm{TN})+(1/\mathrm{FP})+(1/\mathrm{FN})}}$, where a is the inverse of the standard normal cumulative distribution evaluated at $1 - (1 - \mathrm{CI}/2)$, and TP, TN, FP, and FN are the frequencies of true positives, true negatives, false positives, and false negatives, respectively (32) (see Fig. 7 *A*).

A meta-analysis of previously published data (33–36) was used to establish the relationship between microfluidic sorting DORs and DORs based on adherent-cell Young's moduli (see Figs. 8 and S4). For each pair of cell types considered, the soft cell type was taken as condition positive.

RESULTS

Molecular characterization

LECs, central cornea cells, and in-vitro-differentiated LECs (Fig. 2 *A*) were first compared for staining of molecular markers. The stemness of each cell type was assessed based on the percentage of cells that expressed the transcription factor ΔNP63α, a nuclear progenitor marker found in holoclones. In normal central corneal epithelia, ΔNP63α protein expression is abundant in basal cells and decreases with differentiation (15,37,38). As expected, the basal layer of the central cornea exhibited a brighter ΔNP63α than the apical layer (Fig. 2 *B*). Furthermore, the LECs exhibited a significantly higher mean ΔNP63α intensity than the differentiated LECs (9.1% vs. 5.8% dynamic range; Fig. 2, *B* and *D*), indicating that the LECs decreased in stemness over the course of the 4-week in vitro culture. It was determined that 89.9% of the LECs were ΔNP63α^{bright}, as was expected

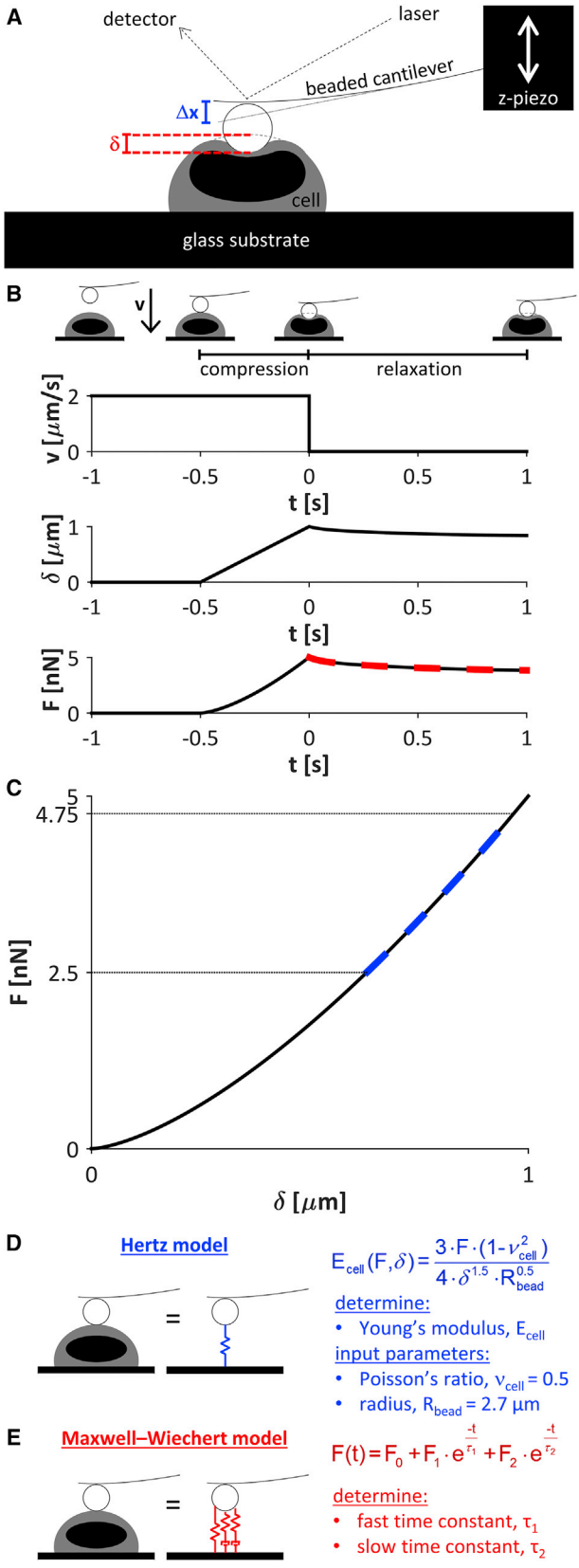

FIGURE 1 AFM. (*A*) A beaded cantilever was used to probe the mechanical properties of individual cells. The positions of the z-piezo and laser were used to calculate the cantilever deflection, Δx, and the indentation, δ. The force, F, exerted on the cell was calculated from the cantilever spring constant, k, by $F = k \cdot \Delta x$. (*B–E*) Mechanical analysis of an idealized cell with an indentation-independent Young's modulus of 1.7 kPa. (*B*) The cantilever was driven toward the cell with a velocity, v, of 2 μm/s. The increase in indentation at $t = -0.5$ s indicated cantilever-cell contact. The driving velocity was maintained to exert a compressive force on the cell until the force trigger of 5 nN was reached, completing the compression segment of the curve. The cantilever position was then maintained on the surface of the cell for 1 s while the unforced cellular relaxation response was recorded (relaxation segment). (*C*) The compression segment of the force-indentation curve was used to determine the cellular Young's modulus, which is directly related to the slope of the curve. (*D*) The Hertzian model, which describes sphere-sphere contact, was employed to calculate the cellular Young's modulus, E. The model was fit to the force-indentation curve over the range of 50–95% force (*C*, *dashed line*). (*E*) The Maxwell-Wiechert model (with 2 Maxwell elements) was fit to the relaxation segment of the force-time curve (*B*, *red dashed line*) to calculate the viscoelastic time constants, τ_1 and τ_2. To see this figure in color, go online.

considering the manufacturer's selection of a ΔNP63$\alpha^{positive}$ cell population (Fig. 2 *D*). After extended culture, only 30.3% of the differentiated LECs were ΔNP63α^{bright} (Fig. 2 *D*), further supporting the successful differentiation of the LECs during extended culture.

Quantification of the DAPI nuclear stain and ABCG2 cytoplasmic stain (Fig. 2 *C*) enabled calculation of the nucleus/cytoplasm ratio, diameter, and aspect ratio for each LEC and differentiated LEC. The nucleus/cytoplasm ratio was significantly higher for the LECs than for the differentiated LECs (Fig. 2 *E*). In agreement with a previous study that specified a nucleus/cytoplasm ratio cutoff of 0.7 (14), 8.1% of the LECs and 0.88% of the differentiated LECs exhibited a high nucleus/cytoplasm ratio. The LECs were significantly smaller than the differentiated LECs (Fig. 2 *F*), but the cellular aspect ratios were not significantly different (Fig. 2 *G*).

Cell mechanics

The LECs exhibited significantly lower Young's moduli than both the central cornea cells and the differentiated LECs (Figs. 3 *B* and 4 *A*), indicating that cell stiffness may be used as a stemness indicator for cells derived from the corneal limbus. The differentiated LECs were significantly larger than the LECs and the central cornea cells, and the LECs were significantly larger than the central cornea cells (Fig. 4 *B*). However, there were no significant differences among the cell populations with respect to the aspect ratio (Fig. 4 *C*) or the fast viscoelastic time constant, τ_1 (Figs. 3 *C* and 4 *D*). The slow viscoelastic time constant, τ_2, was significantly lower for the LECs than for the differentiated LECs (Figs. 3 C and 4 E), indicating a more viscous behavior for the differentiated LECs. However, the slow viscoelastic time constant cannot be regarded as an ideal stemness marker because the difference between the LECs and central cornea cells was not significant. Overall, neither

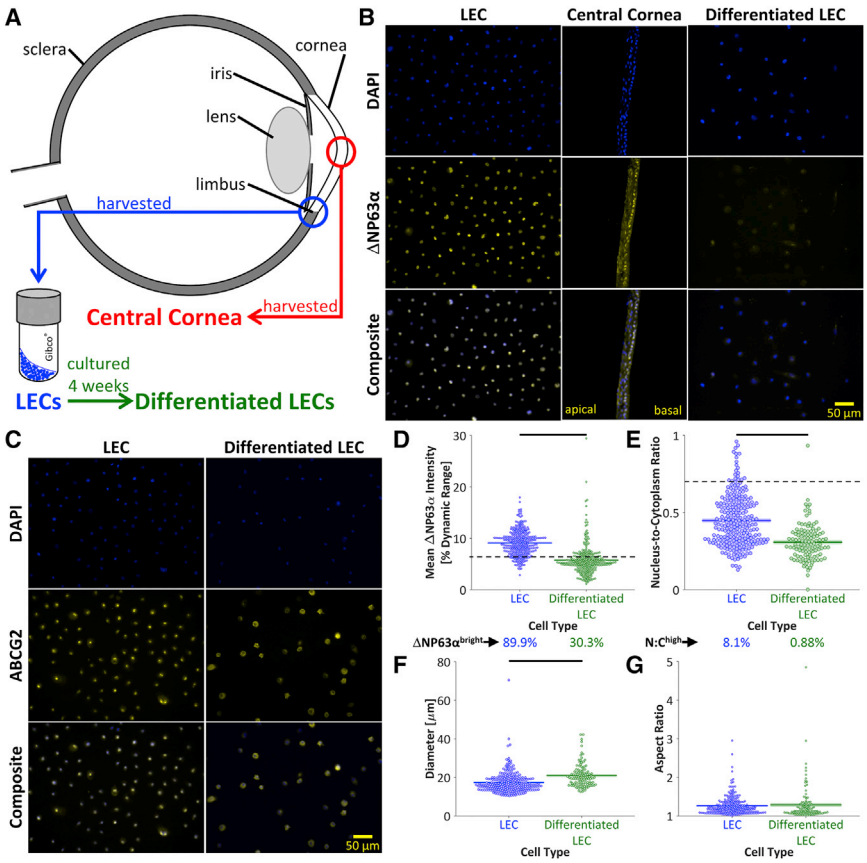

FIGURE 2 Molecular characterization. (*A*) LECs were harvested from the corneal limbus. Differentiated LECs were obtained by culturing the LECs in vitro for 4 weeks. Central cornea cells were harvested from human corneas. (*B*) Dissociated LECs, intact central cornea tissue, and dissociated differentiated LECs were stained for nuclear material (DAPI) and the progenitor marker ΔNP63α. The stem-like LECs stained more brightly for ΔNP63α than the differentiated LECs. The central cornea tissue displayed a basal layer of stem-like ΔNP63α^{bright} cells, whereas the differentiated apical cells were ΔNP63α^{dim}. (*C*) To identify the nuclear and cytoplasmic areas of the dissociated LECs and differentiated LECs, cells were stained for nuclear material (DAPI) and the cell membrane marker ABCG2. Scale bars, 50 μm. (*D*) ΔNP63α was significantly brighter for LECs than differentiated LECs ($p < 10^{-6}$), and a higher percentage of ΔNP63α^{bright} cells was observed in LECs than in differentiated LECs, indicating a decreased percentage of stem-like cells after the 4-week in vitro culture. (*E*) The nucleus/cytoplasm area ratio, as determined by DAPI and ABCG2 staining, was significantly higher in LECs than in differentiated LECs ($p < 10^{-6}$). It was found that 8.1% of LECs and 0.88% of differentiated LECs displayed nucleus/cytoplasm ratios above the previously described threshold of 0.7 (14), further supporting the higher prevalence of stem-like cells in the LEC population. (*F*) The differentiated LECs were significantly larger than the LECs ($p < 10^{-6}$), as quantified by the ABCG2 cytoplasmic stain. (*G*) The aspect ratio was not significantly different between LECs and differentiated LECs ($p = 0.61$). To see this figure in color, go online.

the aspect ratio nor the viscoelastic time constants serve as specific markers of limbal cell stemness.

To investigate the relationship between each pair of mechanical properties, the parameters were compared for each cell type measured (Fig. 5 *A*). Cells with the highest aspect ratios (>2) were observed to have low viscoelastic time constants, and cells with the highest viscoelastic time constants tended to have low aspect ratios (<2). However, no strong relationship was observed for any pair of mechanical parameters (Fig. 5 *B*), suggesting the potential use of multiple parameters in combination to isolate cell populations of interest. There was a significant but weak relationship between the two viscoelastic time constants regardless of whether the cell types were considered together or individually (Fig. 5 *B*). Interestingly, the Young's modulus and diameter were highly negatively correlated for central cornea cells, but not for LECs, differentiated cells, or all cell types considered together (Fig. 5 *B*).

DISCUSSION

In this work, for the first time to our knowledge, the mechanical properties of cells derived from the corneal limbus were characterized. The LECs, which were shown to be stem-like based on the high percentage of ΔNP63α^{bright} cells, were significantly softer than both the central cornea cells and the in-vitro-differentiated LECs. Therefore, cell stiffness can be used as a stemness indicator for cells derived from the corneal limbus.

Previous studies of stem cell mechanics have shown that various properties change during differentiation. Overall, mechanical comparisons of stem cells and their progeny have revealed that cells with epithelial-like morphologies are softer than cells with mesenchymal-like morphologies (22,23). The epithelial-to-mesenchymal transition observed during LEC differentiation, coupled with the finding presented here of a corresponding stiffness increase, further supports the contention that cells with a mesenchymal morphology are stiffer than epithelial cells. In comparison, the mechanical changes are less clear for cell types that remain mesenchymal-like during differentiation, such as mesenchymal stem cell differentiation to osteoblast lineages (20,22,24).

Studies in which corneal cells were grown on substrates of varying stiffnesses support the finding that the stem-like limbal cells are relatively soft. Corneal epithelial cells

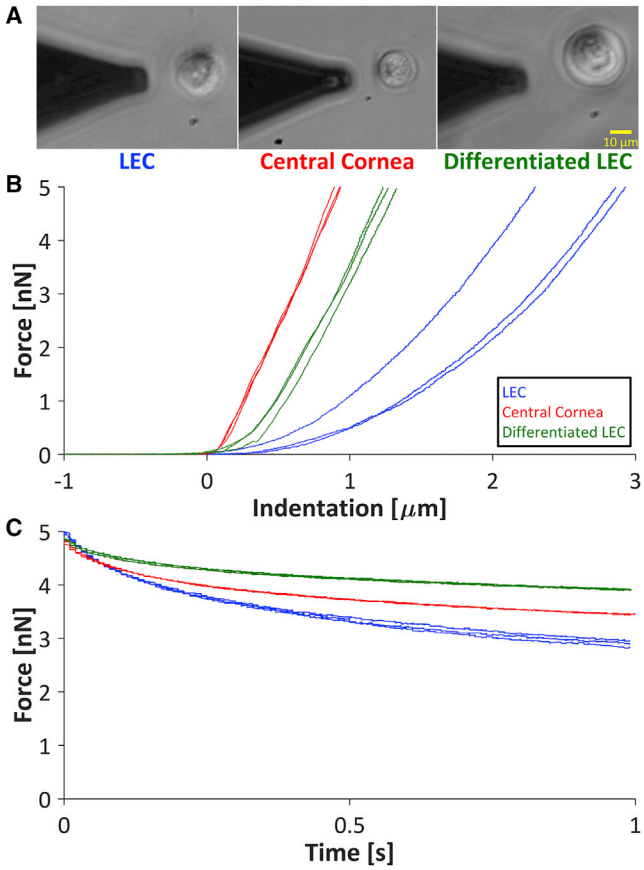

FIGURE 3 Mechanical phenotyping via AFM. (*A*) Phase-contrast microscopy was used both to position the cantilever over each individual cell and to measure the diameter and aspect ratio of each cell. Scale bar, 10 μm. (*B*) Given the direct relationship between the cellular Young's modulus and the slope of the force-indentation curve, representative force-indentation curves indicated that the LECs were softer than the central cornea cells and differentiated LECs. (*C*) Force-time curves obtained during cell relaxation indicated the viscoelastic properties of the cells. The fast viscoelastic time constant, τ_1, which is inversely related to the slope at the minimum time ($t = 0$ s), was similar for all cell types. The slow viscoelastic time constant, τ_2, which is inversely related to the slope at the maximum time ($t = 1$ s), was qualitatively higher for the differentiated LECs than for the LECs and central cornea cells. To see this figure in color, go online.

grown on low-stiffness substrates exhibited the early-differentiation marker cytokeratin 19, whereas cells grown on high-stiffness substrates expressed the late-differentiation markers cytokeratins 3 and 12 (39,40). Furthermore, previous studies indicated that the basement membrane is softer than the apical Bowman's layer (41) and that limbal tissue is softer than central cornea tissue (42). Since cells are known to modulate F-actin organization and thereby alter their stiffness in response to the stiffness of the underlying substrate (43), the finding that the limbal niche is softer than the central cornea niche supports the contention that the Young's modulus results reflect differences between the in vivo mechanical environments of the stem-like and differentiated cell types.

The slow viscoelastic time constant changed during in vitro differentiation, but the fast viscoelastic time constant did not, suggesting that distinct cellular structures may dominantly underpin each viscoelastic time constant. The nucleus is known to be several orders of magnitude more viscous than the cytoskeleton ($\mu_{\text{nucleus}} \approx 5$ kPa-s (44), $\mu_{\text{actin}} \approx$ 1–10 mPa-s (45), $\mu_{\text{microtubule}} \approx$ 1–100 mPa-s (45)). Therefore, the observed increase in nuclear area during in vitro LEC differentiation (Fig. S2) may partially explain the concomitant increase observed in the slow viscoelastic time constant. Furthermore, a recent study of fibroblasts, which also employed a two-time-constant relaxation model, found that the actin network governs relaxation behavior over shorter timescales, whereas the intermediate filament network dictates long-term relaxation (46). Thus, an intermediate filament rearrangement during limbal cell differentiation may play a dominant role in cell relaxation compared with actin rearrangement. Interestingly, cytokeratins 3, 12, and 19, which comprise type I and II intermediate filaments, are commonly used to identify stemness in the limbus (39,40), further emphasizing a potential relationship between the intermediate filament structure and cellular mechanical properties.

The finding that the differentiated LECs were larger than both the LECs and the central cornea cells is supported by the previous observation that cells increased in size over the course of in vitro differentiation due to external stressors and the lack of three-dimensional spatial restrictions (47). The finding that the LECs were larger than the central cornea cells (Fig. 4 *B*) conflicts with a previous study that found that LECs were smaller than central cornea cells (21). However, that study used flow cytometry to measure the size of dissociated cells ex vivo, as well as in vivo confocal microscopy to investigate only the most basal and superficial layers of intact epithelial tissue, whereas the data presented here refer to rounded, immobilized cells that represent the entirety of each anatomical region. Furthermore, the distribution of cell diameters (Fig. 4 *B*) indicates that the LECs include a portion of smaller cells with no counterpart in the central cornea population, which is similar to the previously presented data (21).

Quantification of both the ABCG2 cell membrane stain and the AFM phase-contrast images indicated an increase in cell diameter, with no significant change in the aspect ratio, during in vitro LEC differentiation (Figs. 2, *F* and *G*, and 4, *B* and *C*). Although the LEC diameters were similar (~20 μm) for both methods, quantification of the differentiated LEC phase-contrast images yielded a 50% larger average diameter than quantification of the ABCG2 images. The apparent diameter discrepancy can be explained by differences in the surface coatings, which are known to affect cell morphology (48–51), as cells were plated on poly-L-lysine-coated glass for the phase-contrast images and on uncoated glass for the ABCG2 images.

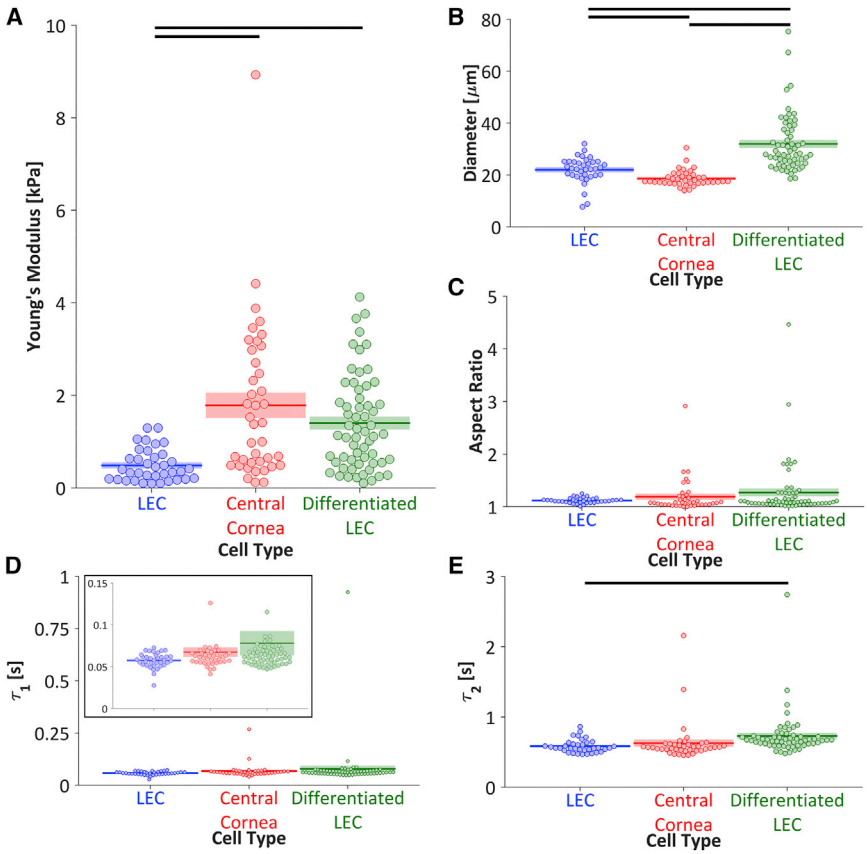

FIGURE 4 Cell mechanics. (*A*) The LECs were significantly softer than both the central cornea cells ($p_{adjusted} = 0.001$) and differentiated LECs ($p_{adjusted} < 10^{-6}$), suggesting that Young's modulus may be used as an indicator for the differentiation state of limbal epithelial cells. (*B*) The LECs were significantly larger than the central cornea cells ($p_{adjusted} < 10^{-6}$) but significantly smaller than the differentiated LECs ($p_{adjusted} < 10^{-6}$). The central cornea cells were significantly smaller than the differentiated LECs ($p_{adjusted} < 10^{-6}$). (*C* and *D*) There were no significant differences in the aspect ratio or the fast viscoelastic time constant, τ_1. (*E*) The LECs had a significantly lower slow viscoelastic time constant, τ_2, than the differentiated LECs ($p_{adjusted} = 0.043$). Due to the nonnormal distribution of each population (Shapiro-Wilk W test, $\alpha = 0.05$), a bootstrapping ANOVA was used to discern statistically significant differences. Populations connected by black bars are significantly different (Holm's adjusted *p*-values, $\alpha = 0.10$). To see this figure in color, go online.

To determine the utility of each mechanical property as a biomarker, we analyzed each parameter as a binary classifier of stemness. For a chosen threshold, a contingency table was constructed to compare the test condition with the actual condition (Fig. 6, *A* and *B*). ROC curves were plotted by calculating the TPR and FPR for the full range of classifier values (Fig. 6 *C*). The parameters that best classified stemness (i.e., separated LECs from differentiated LECs) were

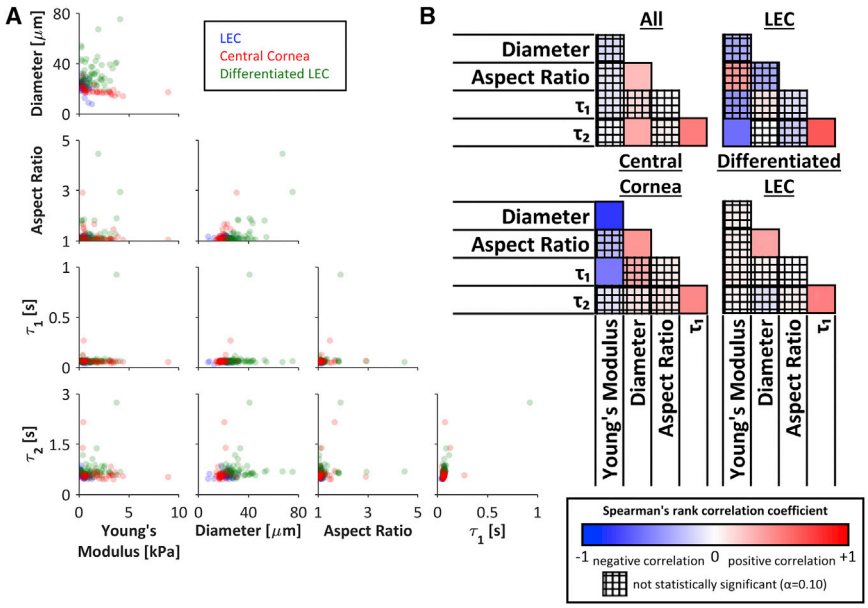

FIGURE 5 Pairwise cell mechanics comparisons. (*A*) The weak relationships between pairs of mechanical properties indicated that each property may be used independently to identify or isolate a cell population of interest (LEC, $n = 36$; central cornea, $n = 40$; differentiated LEC, $n = 60$). (*B*) The pairwise Spearman's correlation coefficients among the five mechanical parameters for all cells (*top left*), LECs only (*top right*), central cornea cells only (*bottom left*), and differentiated LECs only (*bottom right*) indicated that correlations were generally weak or not significant. In all cases, the two viscoelastic parameters were positively associated. Interestingly, the Young's modulus and diameter were highly negatively correlated for central cornea cells, but not for LECs, differentiated cells, or all cell types considered together. Spearman's rank correlation coefficients range from −1 to +1. The crosshatch pattern indicates a correlation that was not statistically significant based on Holm's adjusted *p*-values ($\alpha = 0.10$). To see this figure in color, go online.

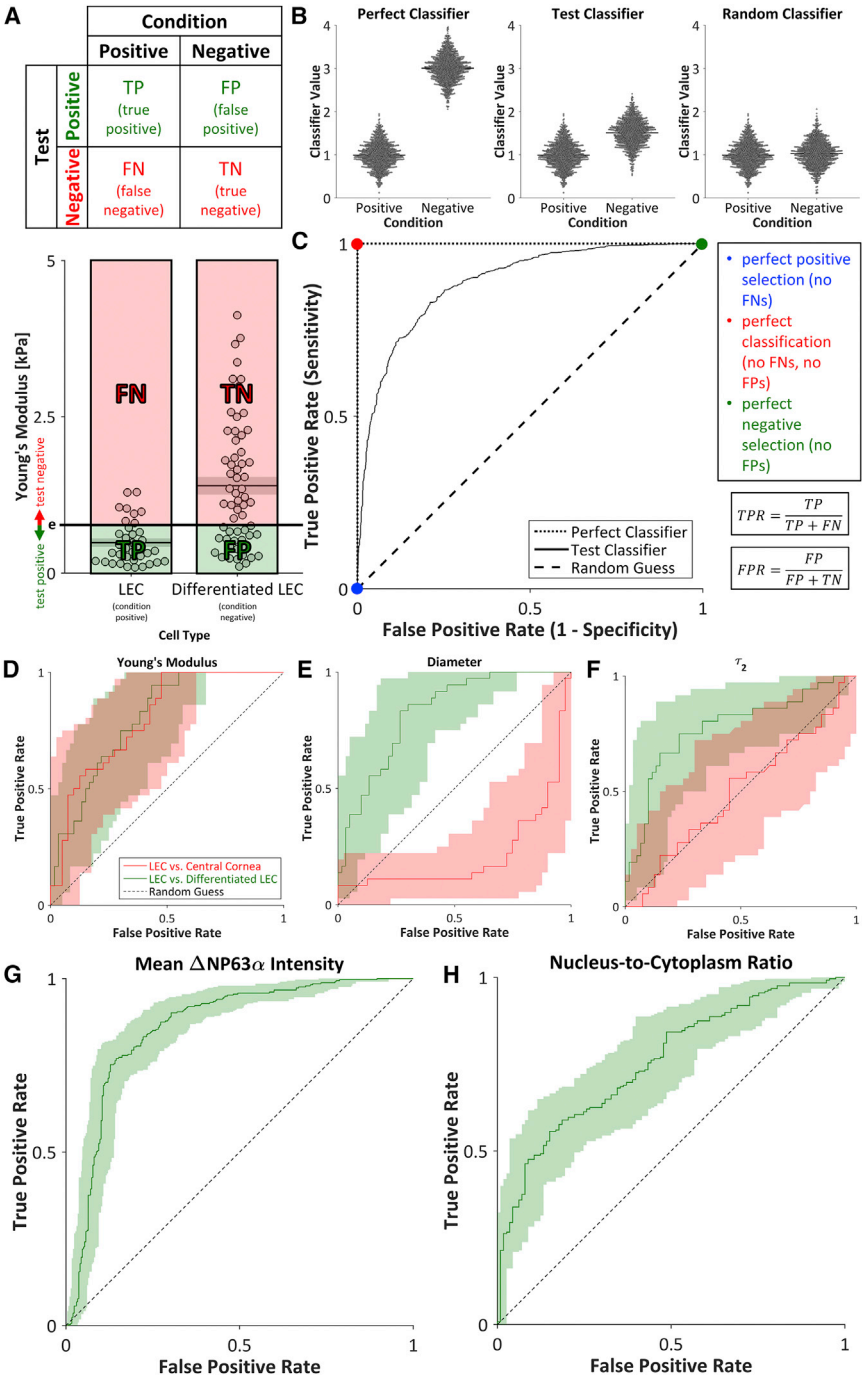

FIGURE 6 ROC curves. (*A*) For a binary classifier, the contingency table separates test subjects into TPs, FPs, FNs, and TNs. Young's modulus was used to select for LECs (condition positive) and against differentiated LECs (condition negative). Cells below and above the threshold Young's modulus (e) were considered to be test positive and test negative, respectively. (*B*) A perfect classifier would enable perfect discrimination between condition-positive and condition-negative cells (no FPs, no FNs), whereas a random classifier would enable no discrimination between condition-positive and condition-negative cells (TPs = FPs, TNs = FNs). In practice, the threshold value of a test classifier can be shifted to improve positive selection at the cost of reduced negative selection, or vice-versa. (*C*) ROC curves (*black lines* and *D–H*) were generated by calculating the TPR and FPR for all possible threshold values. The ROC curve for a test classifier (*solid line*) lies between the ROC curves for a perfect classifier (*dotted line*) and a random guess (*dashed line*). (*D–H*) ROC curves for the selection of LECs against either central cornea cells or differentiated LECs using the test positive conditions of a (*D*) low Young's modulus; (*E*) low diameter; (*F*) low, slow viscoelastic time constant (τ_2); (*G*) high mean ΔNP63α intensity; or (*H*) high nucleus/cytoplasm ratio indicated that each parameter can be used to discern stemness. Shaded regions indicate 95% CI. To see this figure in color, go online.

the Young's modulus (Fig. 6 *D*), diameter (Fig. 6 *E*), slow viscoelastic time constant (Fig. 6 *F*), mean ΔNP63α intensity (Fig. 6 *G*), and nucleus/cytoplasm ratio (Fig. 6 *H*). The aspect ratio (Fig. S3 *A*) and fast viscoelastic time constant (Fig. S3 *B*) did not successfully indicate stemness.

To further understand the binary classification, the DOR was chosen as a single parameter that summarizes the TPR and FPR (Fig. 7 *A*). The Young's modulus performed well in the selection of LECs against both central cornea cells and differentiated LECs (Fig. 7 *B*), but classification on the basis of the diameter or the slow viscoelastic time constant succeeded only in the selection of LECs against differentiated LECs (Fig. 7, *C* and *D*). The maximum DORs for the selection of LECs against differentiated LECs on the basis of the mean ΔNP63α intensity was ~90 (Fig. 7 *E*; Table S1), indicating that the odds of a positive stemness test among LECs is 90 times higher than the odds of a positive stemness test among differentiated

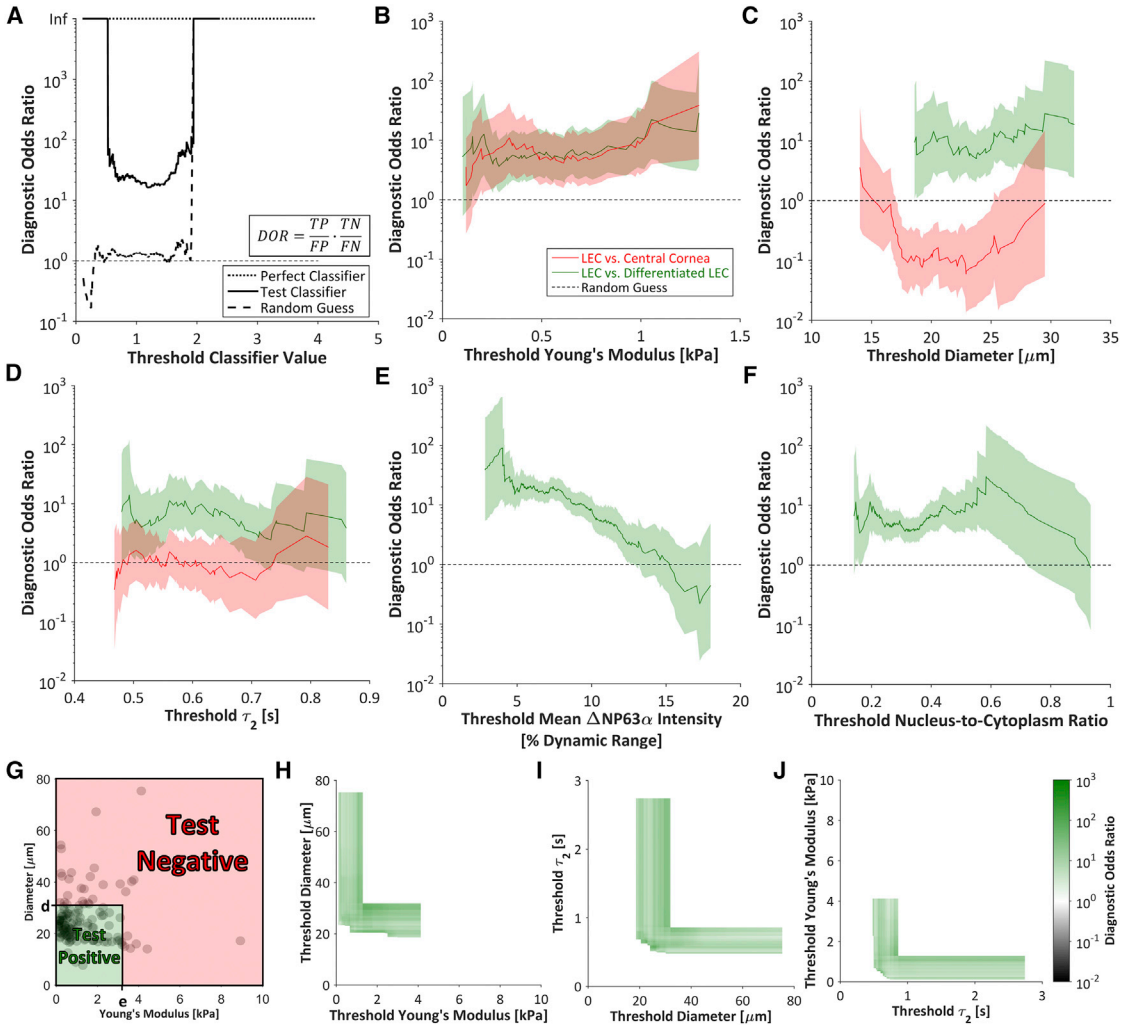

FIGURE 7 DOR. (*A*) The DOR measures the overall utility of a binary classifier by $TP \cdot TN / FP \cdot FN$. The DOR of a perfect classifier (*dotted line*) is infinite for any threshold value, whereas the DOR of a random classifier (*dashed line*) is ~1, and a test classifier (*solid line*) will have a finite DOR of >1. Extreme threshold classifier values yield an infinite DOR (where FP = 0 or FN = 0). (*B–F*) The DORs based on the (*B*) Young's modulus, (*C*) diameter, (*D*) slow viscoelastic time constant, (*E*) mean ΔNP63α intensity, and (*F*) nucleus/cytoplasm ratio were generally higher for the selection of LECs against differentiated LECs than against central cornea cells. The DOR based on the Young's modulus was ~10 regardless of the threshold value. Shaded regions indicate 95% CI. (*G*) To determine the utility of a two-parameter classifier, cells below both the diameter threshold, *d*, and the Young's modulus threshold, *e*, were defined as test positive. All other cells were defined as test negative. (*H–J*) For all possible combinations of (*H*) threshold diameter and threshold Young's modulus, (*I*) threshold slow viscoelastic time constant (τ_2) and threshold diameter, and (*J*) threshold Young's modulus and threshold slow viscoelastic time constant, the DOR was calculated for selection of LECs against differentiated LECs. The increase in DOR upon inclusion of a second classifier indicates that the combined classifiers can outperform the single-parameter classifiers. The DORs ranged from 0.01 to 1000. To see this figure in color, go online.

LECs (32). In comparison, the maximum DOR was ~30 for selection on the basis of the nucleus/cytoplasm ratio, Young's modulus, or diameter, and ~14 for selection on the basis of the slow viscoelastic time constant (Fig. 7, *B–D* and *F*; Table S1). However, the DORs for classification based on the aspect ratio (Fig. S3 *C*; Table S1) or the fast viscoelastic time constant (Fig. S3 *D*; Table S1) were relatively low, further corroborating the finding that the aspect ratio and fast viscoelastic time constant are not suitable stemness indicators.

In addition to the DOR, the area under the ROC curve is commonly used to measure the utility of a classifier. The area under the curve (AUC) data support the DOR-based finding that the mean ΔNP63α intensity, diameter, and Young's modulus best identified LECs from a mixed population containing differentiated LECs (Table S2).

Previous results further support the relationship between adherent-cell AFM and microfluidic sorting ability: mechanics data from adhered cells correlate with sorting trajectories within our device, and cells taken from the outlets of our device display distinct mechanical properties after attachment (34). Specifically, the relatively soft and low-viscosity K562 cells have been efficiently sorted from HL60 cells (sorting DOR = 205 (36)) and leukocytes (sorting

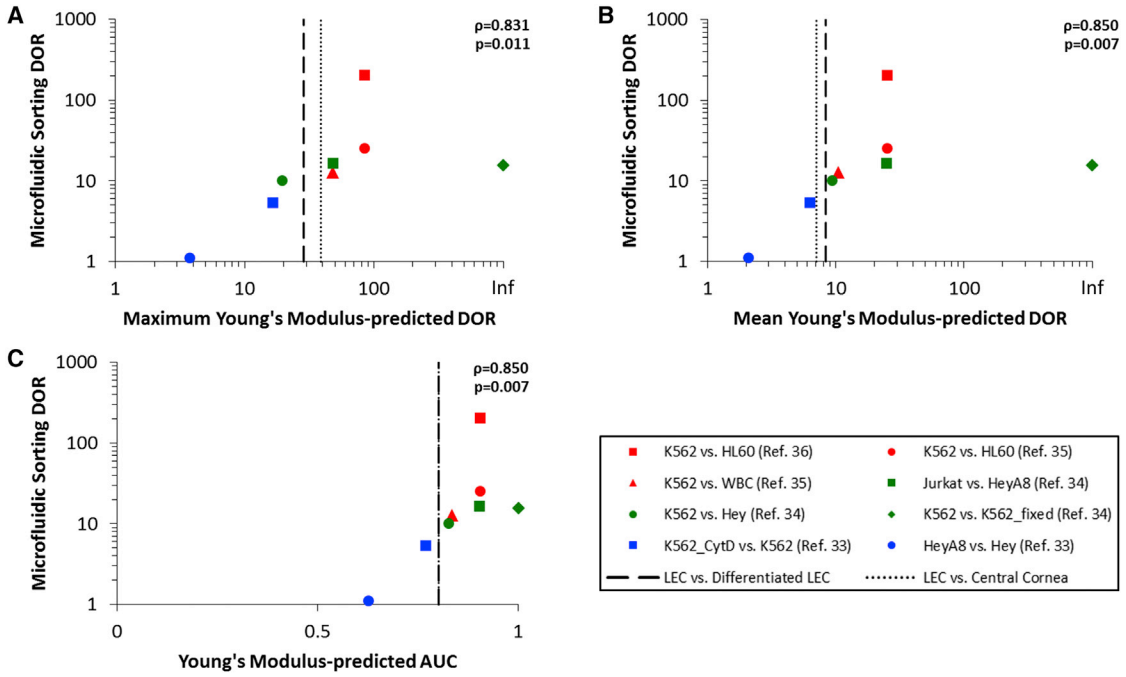

FIGURE 8 Correlation between adherent-cell mechanics and microfluidic sorting. (*A–C*) Sorting for stem-like cells from the limbal region (*black vertical lines*) is projected to yield a microfluidic sorting DOR of ~10, based on positive correlations between microfluidic sorting DORs and either (*A*) the maximum Young's modulus-predicted DOR ($\rho = 0.831$, $p = 0.11$), (*B*) the mean Young's modulus-predicted DOR ($\rho = 0.850$, $p = 0.007$), or (*C*) the AUC of the Young's modulus ROC ($\rho = 0.850$, $p = 0.007$). DORs and AUCs were calculated from previously published data (33–36). Spearman's correlation coefficients were calculated to test for monotonic trends. To see this figure in color, go online.

DOR = 12.7 (35)). The similar relative mechanical properties reported in the limbal system suggest the applicability of microfluidic sorting technology to enrich for limbal stem-like cells.

To quantitatively elucidate the relationship between the adherent-cell Young's modulus-based DOR and sorting ability, a meta-analysis of previously published data was conducted (Figs. 8 and S4). The positive correlations between the microfluidic sorting DORs and the DORs predicted from the Young's modulus (maximum DOR, $\rho = 0.831$, $p = 0.011$; mean DOR, $\rho = 0.850$, $p = 0.007$; AUC, $\rho = 0.850$, $p = 0.007$) provide evidence that the high-Young's-modulus-based DORs observed in the limbal system indicate an ability to enrich for stem-like cells from the limbal niche using microfluidics.

Evaluating parameters on the single-cell level enabled a combined classifier analysis. Thus, given the positive performance of the Young's modulus, diameter, and slow viscoelastic time constant as stemness classifiers, the performance of pairwise classifiers was also assessed. Cells with both parameters below the respective thresholds were taken as test positive, and the remainder were taken as test negative (Fig. 7 *G*). For the Young's modulus, diameter, and slow viscoelastic time constant, the maximum DOR for each pair of parameters exceeded 35 when selecting for LECs and against differentiated LECs, indicating that the combined classifiers have the potential to classify cells more efficiently than the individual parameters (Fig. 7, *H–J*; Table S3). The combined classifiers were less successful in selecting for LECs and against central cornea cells (Fig. S3, *E–G*; Table S3).

Although the DOR provides a measure of the utility of a binary classifier, the calculation assumes that FPs (i.e., differentiated cells that are identified as stem-like cells) and FNs (i.e., stem-like cells that are identified as differentiated cells) are equally problematic. Thus, the ideal scheme to enrich stem-like limbal cells for regenerative medicine does not necessarily maximize the DOR. The presence of stem-like cells in a population may accelerate tissue regeneration (reviewed in (52)), promoting the idea that FNs may be less desirable than FPs. Contrarily, the low prevalence (1–10%) of stem-like cells in the limbus (8,53) adds to the challenge of removing a large percentage of FP cells. Therefore, further biological studies of the limbal niche will be required to determine the relative importance of minimizing FPs versus FNs for applications to corneal regeneration using LSC therapy (8). When the ideal balance between FPs and FNs is determined, the results presented here can be used as a framework to inform the mechanically driven enrichment of stem-like cells from a heterogeneous corneal cell population.

CONCLUSIONS

We identify cell stiffness as a stemness indicator, which is a novel finding, to our knowledge, for cells derived from the

corneal limbus. Our characterization of the mechanical properties of cells derived from the corneal limbus showed that stem-like LECs were softer than cells from the central cornea as well as in-vitro-differentiated LECs. Additional biophysical properties, such as size and the slow viscoelastic time constant, can also be utilized to distinguish stem-like LECs from a mixed cell population.

Biophysical markers hold great promise for improving corneal transplant success for LSCD patients. Whereas measuring cellular mechanical properties by AFM is a low-throughput process (~3 min/cell), microfluidics promises to provide a high-throughput method that combines stiffness-, size-, and viscoelasticity-based sorting to isolate stem-like cells (34–36,54–56). Such high-throughput techniques can be used to generate corneal tissue implants with highly enriched stem-like limbal cell populations, which may yield superior clinical outcomes compared with tissue implants that are directly harvested from the cornea (8).

SUPPORTING MATERIAL

Four figures and three tables are available at http://www.biophysj.org/biophysj/supplemental/S0006-3495(16)30771-8.

AUTHOR CONTRIBUTIONS

T.B. designed and performed research, analyzed data, and wrote the manuscript. J.L.C. designed and performed research, and wrote the manuscript. J.D.L. and T.S. designed research and wrote the manuscript.

ACKNOWLEDGMENTS

The authors thank James Wade for assistance with ROC analysis, Wenwei Xu for assistance with AFM, and Todd McDevitt and Andrés García for helpful discussions.

This work was supported by grants from the National Institute of General Medical Sciences, National Institutes of Health (Biotechnology Training Grant on Cell and Tissue Engineering, T32 GM008433 to T.B.); the Knights Templar Eye Foundation (to J.L.C.); the Center for Regenerative Engineering and Medicine (to J.D.L. and T.S.); the Sharon Stewart Aniridia Research Trust (to J.D.L.); and the Civil, Mechanical and Manufacturing Innovation Division, National Science Foundation (1538161 to T.S.).

REFERENCES

1. Tseng, S. C. 1989. Concept and application of limbal stem cells. *Eye (Lond.).* 3:141–157.
2. Schlötzer-Schrehardt, U., and F. E. Kruse. 2005. Identification and characterization of limbal stem cells. *Exp. Eye Res.* 81:247–264.
3. Dua, H. S., and A. Azuara-Blanco. 2000. Limbal stem cells of the corneal epithelium. *Surv. Ophthalmol.* 44:415–425.
4. Ahmad, S. 2012. Concise review: limbal stem cell deficiency, dysfunction, and distress. *Stem Cells Transl. Med.* 1:110–115.
5. He, H., and S. C. Yiu. 2014. Stem cell-based therapy for treating limbal stem cells deficiency: a review of different strategies. *Saudi J. Ophthalmol.* 28:188–194.
6. Holland, E. J., A. R. Djalilian, and G. S. Schwartz. 2003. Management of aniridic keratopathy with keratolimbal allograft: a limbal stem cell transplantation technique. *Ophthalmology.* 110:125–130.
7. Pellegrini, G., P. Rama, …, M. De Luca. 2013. Biological parameters determining the clinical outcome of autologous cultures of limbal stem cells. *Regen. Med.* 8:553–567.
8. Rama, P., S. Matuska, …, G. Pellegrini. 2010. Limbal stem-cell therapy and long-term corneal regeneration. *N. Engl. J. Med.* 363:147–155.
9. Pellegrini, G., C. E. Traverso, …, M. De Luca. 1997. Long-term restoration of damaged corneal surfaces with autologous cultivated corneal epithelium. *Lancet.* 349:990–993.
10. Tan, D. T., L. A. Ficker, and R. J. Buckley. 1996. Limbal transplantation. *Ophthalmology.* 103:29–36.
11. Ksander, B. R., P. E. Kolovou, …, N. Y. Frank. 2014. ABCB5 is a limbal stem cell gene required for corneal development and repair. *Nature.* 511:353–357.
12. Truong, T. T., K. Huynh, …, S. X. Deng. 2011. SSEA4 is a potential negative marker for the enrichment of human corneal epithelial stem/progenitor cells. *Invest. Ophthalmol. Vis. Sci.* 52:6315–6320.
13. Ahmad, S., S. Kolli, …, M. Lako. 2008. A putative role for RHAMM/HMMR as a negative marker of stem cell-containing population of human limbal epithelial cells. *Stem Cells.* 26:1609–1619.
14. Arpitha, P., N. V. Prajna, …, V. Muthukkaruppan. 2005. High expression of p63 combined with a large N/C ratio defines a subset of human limbal epithelial cells: implications on epithelial stem cells. *Invest. Ophthalmol. Vis. Sci.* 46:3631–3636.
15. Pellegrini, G., E. Dellambra, …, M. De Luca. 2001. p63 identifies keratinocyte stem cells. *Proc. Natl. Acad. Sci. USA.* 98:3156–3161.
16. Funderburgh, M. L., Y. Du, …, J. L. Funderburgh. 2005. PAX6 expression identifies progenitor cells for corneal keratocytes. *FASEB J.* 19:1371–1373.
17. Hipfner, D. R., Q. Mao, …, S. P. Cole. 1999. Monoclonal antibodies that inhibit the transport function of the 190-kDa multidrug resistance protein, MRP. Localization of their epitopes to the nucleotide-binding domains of the protein. *J. Biol. Chem.* 274:15420–15426.
18. Özvegy-Laczka, C., G. Várady, …, B. Sarkadi. 2005. Function-dependent conformational changes of the ABCG2 multidrug transporter modify its interaction with a monoclonal antibody on the cell surface. *J. Biol. Chem.* 280:4219–4227.
19. Deonarain, M. P., C. A. Kousparou, and A. A. Epenetos. 2009. Antibodies targeting cancer stem cells: a new paradigm in immunotherapy? *MAbs.* 1:12–25.
20. Bongiorno, T., J. Kazlow, …, T. Sulchek. 2014. Mechanical stiffness as an improved single-cell indicator of osteoblastic human mesenchymal stem cell differentiation. *J. Biomech.* 47:2197–2204.
21. Romano, A. C., E. M. Espana, …, S. C. G. Tseng. 2003. Different cell sizes in human limbal and central corneal basal epithelia measured by confocal microscopy and flow cytometry. *Invest. Ophthalmol. Vis. Sci.* 44:5125–5129.
22. Darling, E. M., M. Topel, …, F. Guilak. 2008. Viscoelastic properties of human mesenchymally-derived stem cells and primary osteoblasts, chondrocytes, and adipocytes. *J. Biomech.* 41:454–464.
23. Pillarisetti, A., J. P. Desai, …, C. L. Keefer. 2011. Mechanical phenotyping of mouse embryonic stem cells: increase in stiffness with differentiation. *Cell. Reprogram.* 13:371–380.
24. Yourek, G., M. A. Hussain, and J. J. Mao. 2007. Cytoskeletal changes of mesenchymal stem cells during differentiation. *ASAIO J.* 53:219–228.
25. Barrandon, Y., and H. Green. 1987. Three clonal types of keratinocyte with different capacities for multiplication. *Proc. Natl. Acad. Sci. USA.* 84:2302–2306.
26. Meyer-Blazejewska, E. A., F. E. Kruse, …, U. Schlötzer-Schrehardt. 2010. Preservation of the limbal stem cell phenotype by appropriate culture techniques. *Invest. Ophthalmol. Vis. Sci.* 51:765–774.

27. Carpenter, A. E., T. R. Jones, …, D. M. Sabatini. 2006. CellProfiler: image analysis software for identifying and quantifying cell phenotypes. *Genome Biol.* 7:R100.

28. Jones, T. R., A. Carpenter, and P. Golland. 2005. Voronoi-based segmentation of cells on image manifolds. *In* Computer Vision for Biomedical Image Applications. Y. Liu, T. Jiang, and C. Zhang, editors. Berlin/Heidelberg, Springer, pp. 535–543.

29. Sader, J. E., I. Larson, and P. Mulvaney. 1995. Method for the calibration of atomic force microscope cantilevers. *Rev. Sci. Instrum.* 66:3789–3798.

30. Xu, W., N. Chahine, and T. Sulchek. 2011. Extreme hardening of PDMS thin films due to high compressive strain and confined thickness. *Langmuir.* 27:8470–8477.

31. Shen, Z. L., H. Kahn, …, S. J. Eppell. 2011. Viscoelastic properties of isolated collagen fibrils. *Biophys. J.* 100:3008–3015.

32. Glas, A. S., J. G. Lijmer, …, P. M. M. Bossuyt. 2003. The diagnostic odds ratio: a single indicator of test performance. *J. Clin. Epidemiol.* 56:1129–1135.

33. Wang, G. 2015. Microfluidic cell separation based on cell stiffness. PhD dissertation. Georgia Institute of Technology, Atlanta, Georgia.

34. Wang, G., W. Mao, …, T. Sulchek. 2013. Stiffness dependent separation of cells in a microfluidic device. *PLoS One.* 8:e75901.

35. Wang, G., K. Crawford, …, T. Sulchek. 2015. Microfluidic cellular enrichment and separation through differences in viscoelastic deformation. *Lab Chip.* 15:532–540.

36. Wang, G., C. Turbyfield, …, T. Sulchek. 2015. Cellular enrichment through microfluidic fractionation based on cell biomechanical properties. *Microfluid. Nanofluidics.* 19:987–993.

37. Chen, Z., C. S. de Paiva, …, D.-Q. Li. 2004. Characterization of putative stem cell phenotype in human limbal epithelia. *Stem Cells.* 22:355–366.

38. Joseph, A., A. O. Powell-Richards, …, H. S. Dua. 2004. Epithelial cell characteristics of cultured human limbal explants. *Br. J. Ophthalmol.* 88:393–398.

39. Moers, K., T. Steinberg, …, P. Eberwein. 2013. Substrate elasticity as biomechanical modulator of tissue homeostatic parameters in corneal keratinocytes. *Exp. Cell Res.* 319:1889–1901.

40. Chen, B., R. R. Jones, …, S. G. Alcock. 2012. The mechanical properties of amniotic membrane influence its effect as a biomaterial for ocular surface repair. *Soft Matter.* 8:8379–8387.

41. Last, J. A., S. M. Thomasy, …, C. J. Murphy. 2012. Compliance profile of the human cornea as measured by atomic force microscopy. *Micron.* 43:1293–1298.

42. Philipp, E., N. Jiri, and S. Günther. 2014. Nanoindentation derived mechanical properties of the corneoscleral rim of the human eye. *Key Eng. Mater.* 606:117–120.

43. Solon, J., I. Levental, …, P. A. Janmey. 2007. Fibroblast adaptation and stiffness matching to soft elastic substrates. *Biophys. J.* 93:4453–4461.

44. Guilak, F., J. R. Tedrow, and R. Burgkart. 2000. Viscoelastic properties of the cell nucleus. *Biochem. Biophys. Res. Commun.* 269:781–786.

45. Wagner, O., J. Zinke, …, J. Bereiter-Hahn. 1999. Viscoelastic properties of f-actin, microtubules, f-actin/α-actinin, and f-actin/hexokinase determined in microliter volumes with a novel nondestructive method. *Biophys. J.* 76:2784–2796.

46. Fallqvist, B., M. L. Fielden, …, A. K. B. Gad. 2016. Experimental and computational assessment of F-actin influence in regulating cellular stiffness and relaxation behaviour of fibroblasts. *J. Mech. Behav. Biomed. Mater.* 59:168–184.

47. Rubin, H. 1997. Cell aging in vivo and in vitro. *Mech. Ageing Dev.* 98:1–35.

48. García, A. J., M. D. Vega, and D. Boettiger. 1999. Modulation of cell proliferation and differentiation through substrate-dependent changes in fibronectin conformation. *Mol. Biol. Cell.* 10:785–798.

49. Liberio, M. S., M. C. Sadowski, …, C. C. Nelson. 2014. Differential effects of tissue culture coating substrates on prostate cancer cell adherence, morphology and behavior. *PLoS One.* 9:e112122.

50. Yeung, T., P. C. Georges, …, P. A. Janmey. 2005. Effects of substrate stiffness on cell morphology, cytoskeletal structure, and adhesion. *Cell Motil. Cytoskeleton.* 60:24–34.

51. Sordel, T., F. Kermarec-Marcel, …, N. Picollet-D'hahan. 2007. Influence of glass and polymer coatings on CHO cell morphology and adhesion. *Biomaterials.* 28:1572–1584.

52. Baraniak, P. R., and T. C. McDevitt. 2010. Stem cell paracrine actions and tissue regeneration. *Regen. Med.* 5:121–143.

53. Shaharuddin, B., I. Harvey, …, A. Meeson. 2014. Characterisation of human limbal side population cells isolated using an optimised protocol from an immortalised epithelial cell line and primary limbal cultures. *Stem Cell Rev.* 10:240–250.

54. Tasadduq, B., G. Wang, …, T. Sulchek. 2015. Three-dimensional particle tracking in microfluidic channel flow using in and out of focus diffraction. *Flow Meas. Instrum.* 45:218–224.

55. Hur, S. C., N. K. Henderson-MacLennan, …, D. Di Carlo. 2011. Deformability-based cell classification and enrichment using inertial microfluidics. *Lab Chip.* 11:912–920.

56. Otto, O., P. Rosendahl, …, J. Guck. 2015. Real-time deformability cytometry: on-the-fly cell mechanical phenotyping. *Nat. Methods.* 12:199–202, 4, 202.

Biophysical Journal, Volume *111*

Supplemental Information

Cellular Stiffness as a Novel Stemness Marker in the Corneal Limbus

Tom Bongiorno, Jena L. Chojnowski, James D. Lauderdale, and Todd Sulchek

FIGURES

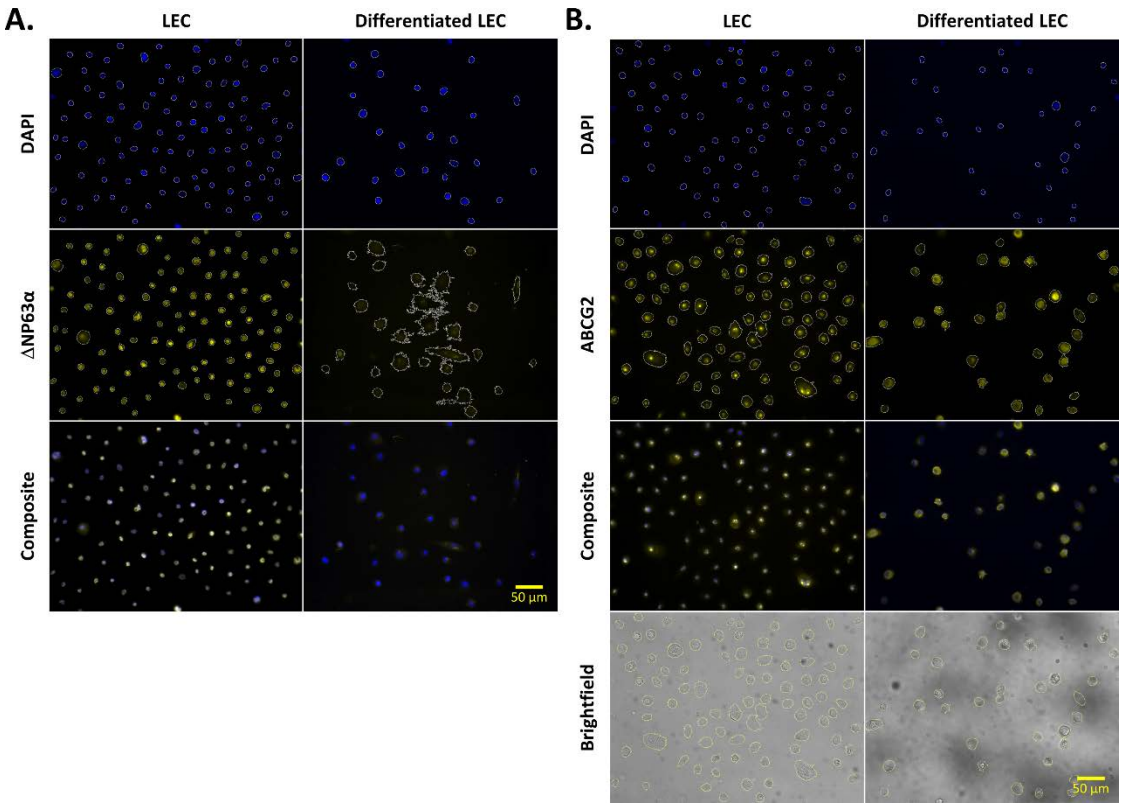

Figure S1. Image Quantification. The nuclei of limbal epithelial cells (LECs) and differentiated LECs were first stained with DAPI to serve as a seed for the identification of individual cells. The seeds were used to identify either the ΔNP63α-stained area (panel A, second row, white outlines), as identified by ΔNP63α intensity (yellow), or the cytoplasmic area (panel B, second row, white outlines), as identified by ABCG2 (yellow). The cellular boundaries are similar whether defined by the brightfield images or the automatically identified cytoplasmic areas (panel B, fourth row, yellow outlines). Scale bars, 50 µm.

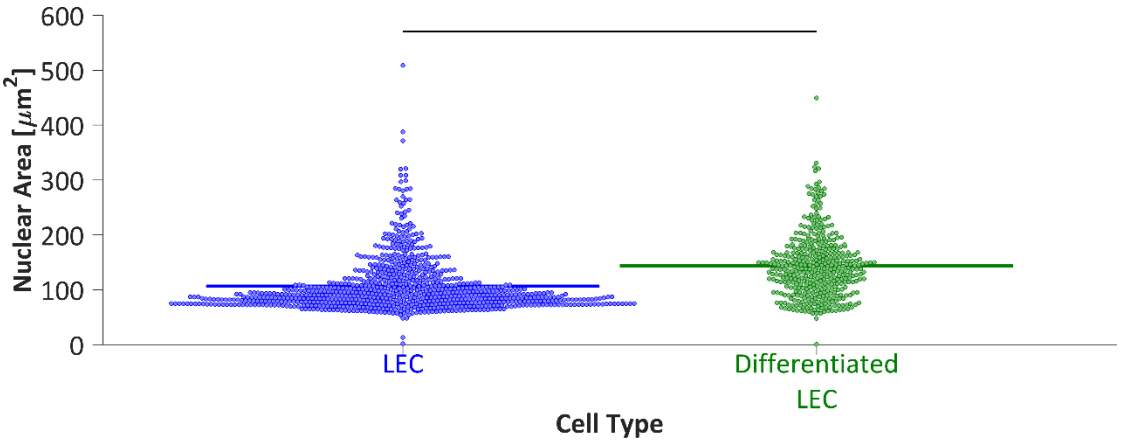

Figure S2. Nuclear Area. The nuclear area, as measured from DAPI channel images taken during ΔNP63α and ABCG2 staining, was significantly higher for differentiated LECs than LECs ($p<10^{-6}$).

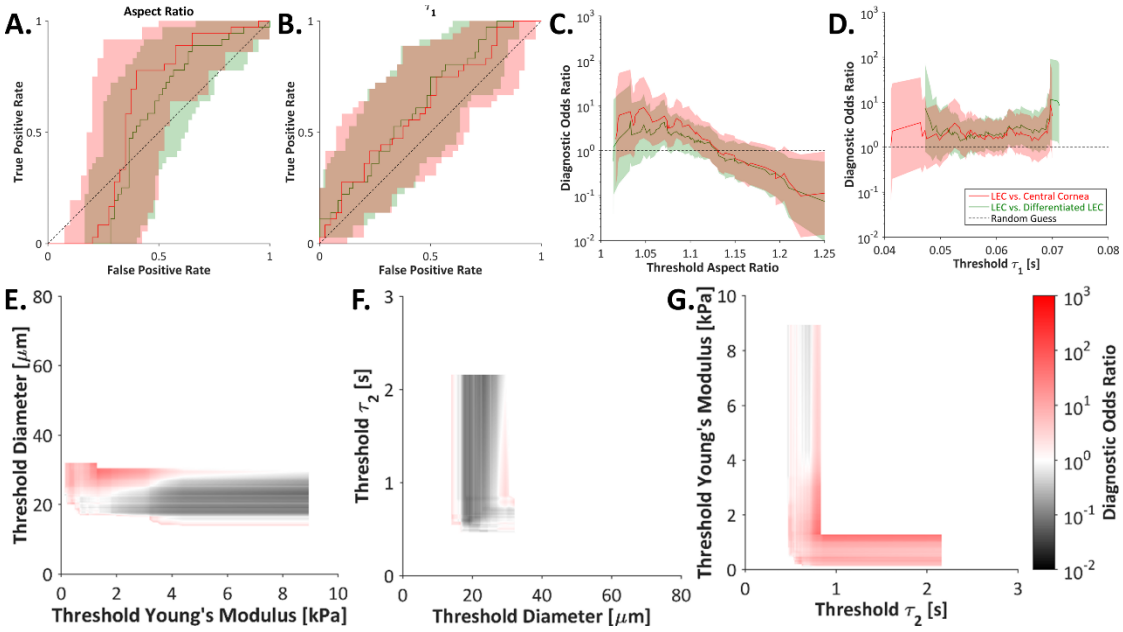

Figure S3. Receiver Operating Characteristic (ROC) Curves. A-B) Selection for limbal epithelial cells (LECs) against central cornea cells (red) or differentiated LECs (green) on the basis of A) aspect ratio and B) the fast viscoelastic time constant (τ_1) was poor, as indicated by areas under the curve of only marginally greater than 0.5, which is the area under the curve for a random classifier. **C-D)** The low diagnostic odds ratios (DORs) for classifiers based on C) the aspect ratio and D) the fast viscoelastic time constant further indicate the poor quality of classification. **E-G)** For all possible combinations of E) threshold diameter and threshold Young's modulus, F) threshold slow viscoelastic time constant (τ_2) and threshold diameter, and G) threshold Young's modulus and threshold slow viscoelastic time constant, the DOR was calculated for selection of LECs against central cornea cells. Overall, the DORs were lower for selection of LECs against central cornea cells than against differentiated LECs (Figs. 7H-J). The DORs ranged from 0.01 (black) to 1 (white) to 1000 (bright red).

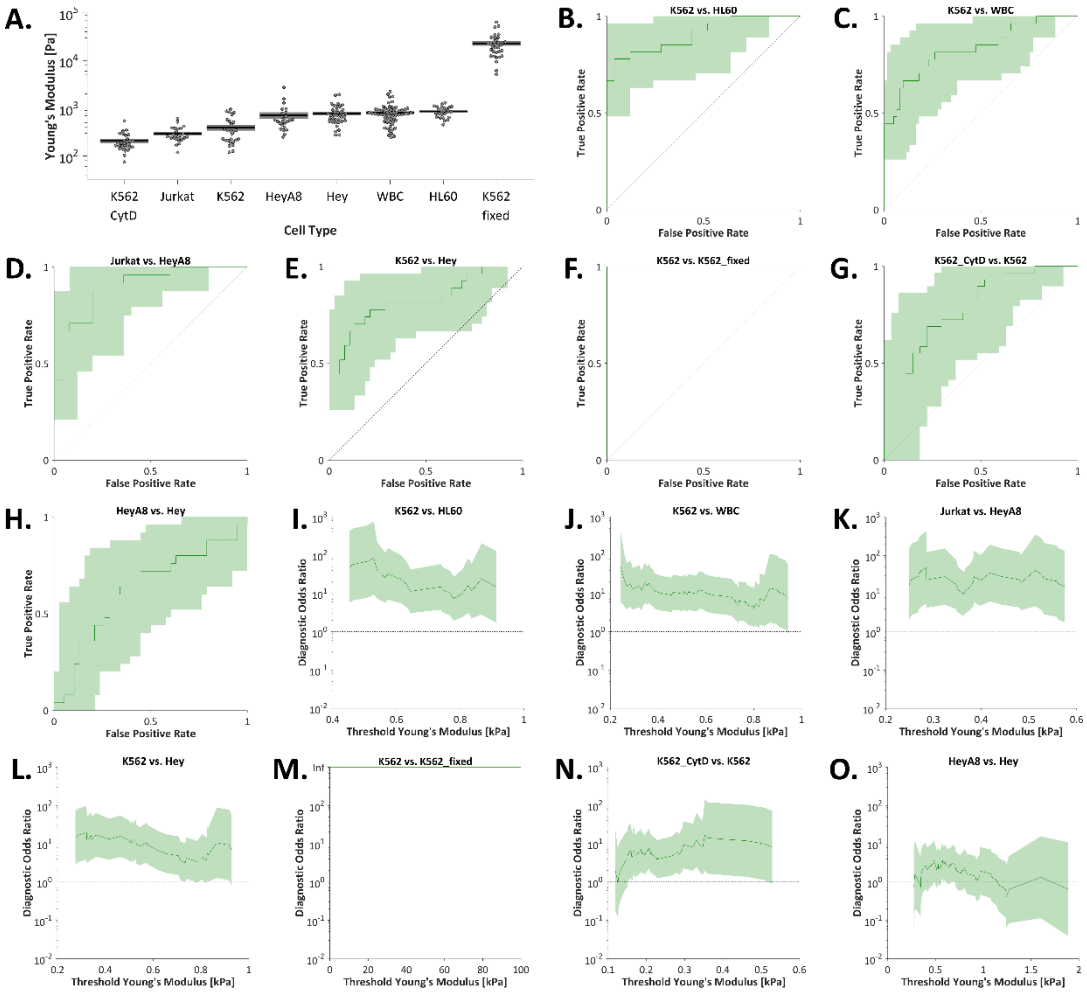

Figure S4. Differences in Adherent Cell Young's Moduli are Correlated with the Microfluidic Sorting Diagnostic Odds Ratio. A. Cellular Young's moduli ranged from 0.1-100 kPa for cell lines previously sorted using microfluidic technology. **B-H.** For various combinations of cell types, the receiver operating curves based on adherent-cell Young's modulus yielded areas under the curve ranging from 0.626 (H, HeyA8 vs. Hey) to 1 (F, K562 vs. K562_fixed), where the soft cell type was taken as condition positive. **I-O.** The maximum diagnostic odds ratio (DOR) based on adherent-cell Young's modulus ranged from 3.713 (O, HeyA8 vs. Hey) to infinity (M, K562 vs. K562_fixed). Shaded regions indicate 95% confidence interval. WBC, white blood cell; fixed, treatment with 4% paraformaldehyde; CytD, treatment with 2 μM cytochalasin-D. Pre-sort Young's moduli of various cell types (Panel B) replotted from (33-36). Young's modulus ROC and DOR curves (C-J) calculated from previously published data (33-36).

TABLES

Table S1. Diagnostic Odds Ratios for Single Parameters. For each parameter, the maximum and mean diagnostic odds ratios (DORs) were calculated for classifying limbal epithelial cells (LECs) versus differentiated LECs or central cornea cells. The DOR of a perfect classifier is infinite for any threshold value, whereas the DOR of a random classifier is approximately 1, and a test classifier will have a finite DOR>1. τ_1, fast viscoelastic time constant; τ_2, slow viscoelastic time constant.

	Maximum DOR		**Mean DOR**	
	LEC vs. Differentiated LEC	**LEC vs. Central Cornea**	**LEC vs. Differentiated LEC**	**LEC vs. Central Cornea**
Mean ΔNP63α Intensity	89.92		16.82	
Nucleus-to-Cytoplasm Ratio	30.44		7.80	
Young's Modulus	28.64	38.68	8.30	7.11
Diameter	28.64	3.55	11.31	0.28
Aspect Ratio	4.62	9.15	1.94	2.96
τ_1	11.67	8.75	2.75	2.31
τ_2	14.24	2.84	6.37	1.03

Table S2. Area under the Receiver Operating Curves. For each parameter, the area under the receiver operating curve was calculated for classifying limbal epithelial cells (LECs) versus differentiated LECs or central cornea cells. The area under the curve of a useful test ranges from 0.5 (random classification) to 1 (perfect classification). τ_1, fast viscoelastic time constant; τ_2, slow viscoelastic time constant; CI, confidence interval.

	LEC vs. Differentiated LEC			**LEC vs. Central Cornea**		
	Area Under Curve	**Lower 95% CI**	**Upper 95% CI**	**Area Under Curve**	**Lower 95% CI**	**Upper 95% CI**
Mean ΔNP63α Intensity	0.860	0.800	0.913			
Nucleus-to-Cytoplasm Ratio	0.757	0.654	0.847			
Young's Modulus	0.801	0.626	0.928	0.802	0.607	0.943
Diameter	0.827	0.654	0.947	0.216	0.051	0.422
Aspect Ratio	0.531	0.344	0.725	0.597	0.381	0.805
τ_1	0.637	0.422	0.823	0.615	0.370	0.827
τ_2	0.777	0.578	0.931	0.500	0.263	0.743

Table S3. Diagnostic Odds Ratios for Two-Parameter Combinations. For each pair of parameters, the maximum and mean diagnostic odds ratios (DORs) were calculated for classifying limbal epithelial cells (LECs) versus differentiated LECs or central cornea cells. The DOR of a perfect classifier is infinite for any threshold value, whereas the DOR of a random classifier is approximately 1, and a test classifier will have a finite DOR>1. τ_2, slow viscoelastic time constant.

	Maximum DOR		**Mean DOR**	
	LEC vs. Differentiated LEC	**LEC vs. Central Cornea**	**LEC vs. Differentiated LEC**	**LEC vs. Central Cornea**
Diameter + Young's Modulus	65.00	42.78	11.89	1.33
τ_2 + Diameter	73.75	3.55	12.23	0.39
Young's Modulus + τ_2	37.55	47.35	8.67	2.74